

Force balances in strong-field magnetoconvection simulationsImogen G. Cresswell ¹, Evan H. Anders ², Benjamin P. Brown ¹,
Jeffrey S. Oishi ³ and Geoffrey M. Vasil ^{4,5}¹*Department of Astrophysical & Planetary Science, University of Colorado, Boulder, Colorado 80309, USA*²*CIERA, Northwestern University, Evanston, Illinois 60201, USA*³*Bates College Department of Physics and Astronomy, Lewiston, Maine 04240, USA*⁴*University of Sydney School of Mathematics and Statistics, Sydney, New South Wales 2006, Australia*⁵*School of Mathematics, University of Edinburgh, Edinburgh EH9 3JZ, United Kingdom*

(Received 20 October 2022; accepted 31 July 2023; published 14 September 2023)

Convection and strong magnetic fields interact in the Sun's envelope and produce many magnetic features. In sunspots, the most intense of these structures, magnetic fields are strong enough to inhibit convection. In this work, we study simulations of magneto-hydrodynamic Rayleigh-Bénard convection (RBC) using the Dedalus pseudospectral framework. We perform a suite of two- and three-dimensional simulations in which we vary the strength of the background magnetic field and the strength of convective driving (quantified, respectively, by the Chandrasekhar number, Q , and the Rayleigh number, Ra). We directly measure and report force balances between the Lorentz, buoyancy, and inertial forces to quantify magnetic constraint. In addition, we measure the solenoidal portion of the force by removing contributions to the pressure gradient to directly study the acceleration responsible for modifying the fluid velocity. We find three simulation regimes: a “constrained” regime where the background magnetic field dominates, a “magnetically influenced” regime where nonlinear Lorentz and inertial forces balance, and a transitional regime between the two. We find the constrained regime only becomes turbulent for large $Q \gtrsim 10^{10}$. Magnetic field fluctuations scale as $B \propto RaQ^{-7/6}$ in constrained regimes and scale as $B \propto Ra^{7/16}Q^{-1/2}$ in the magnetically influenced regime. The efficiency of convection quantified by the Nusselt number scales as the expected $Nu \propto Ra$ in the constrained regime, but a classical hydrodynamic RBC scaling of $Nu \propto Ra^{2/7}$ is found in the magnetically influenced regime even when the nonlinear Lorentz force heavily influences dynamics.

DOI: [10.1103/PhysRevFluids.8.093503](https://doi.org/10.1103/PhysRevFluids.8.093503)**I. INTRODUCTION**

Convection is ubiquitous in magnetized astrophysical and geophysical environments including the surface of low-mass stars, cores of high-mass stars, supernova explosions, accretion disks, and planetary cores [1–5]. In stars, magnetic fields are often generated by a convectively driven dynamo [6]. These dynamogenerated fields interact with surface convection in stars like the Sun and produces a rich variety of observable magnetic structures [7–10]. In the quiet (weakly magnetized) Sun, convective motions sweep and concentrate the magnetic field into cool intergranular lanes in a process known as magnetic flux expulsion [11]. This results in locally strong

Published by the American Physical Society under the terms of the [Creative Commons Attribution 4.0 International](https://creativecommons.org/licenses/by/4.0/) license. Further distribution of this work must maintain attribution to the author(s) and the published article's title, journal citation, and DOI.

magnetic flux tubes that act like fiber optic cables, decreasing the optical depth compared to the surroundings and manifesting as bright points in the dark intergranular lanes [12,13]. The largest and most intense magnetic flux tubes manifest as sunspots where the magnetic fields are strong enough to inhibit convection causing them to appear dark [14,15]. Despite this, heat transport in sunspots is still convective in nature, as observed brightness is too high to be due to radiative transport alone [16]. Small bright features called umbral dots are a signature of strong-field magnetoconvection transporting energy inside sunspots [17,18]. Understanding the behavior of convection in the presence of strong magnetic fields is crucial to understanding these solar magnetic structures.

Numerical simulations of magnetoconvection provide deeper understanding into the physical processes involved; either through multiphysics simulations that include the effects of ionization and radiative transfer [19], or idealized models which neglect these effects in favor of a more fundamental understanding of magnetoconvection [20,21]. Multiphysics simulations of sunspots have shown convective energy transport is dominated by narrow, constrained, convective patterns and identify bright features that can be compared to umbral dot observations [17,22]. Idealized models in both Boussinesq [11,23] and fully compressible systems [7,24,25] have identified different regimes of convective patterns that depend on magnetic field strength. When the background field is large, convection is constrained to follow field lines. Reducing the strength of the background field results in more vigorous convection that can concentrate the magnetic flux to the sides of the cells.

Strong magnetic fields constrain convection in a manner similar to rapid rotation. “Unconstrained” hydrodynamic convection is characterized by flows which are driven by buoyant heating or cooling and nonlinearly deflected by advection. An invariant external process like planetary rotation or a strong magnetic field can impose a strong force on the fluid, and when this force is sufficiently strong, we call the convection “constrained.” In a constrained state, the primary force balance between advection and buoyancy is altered and the convective flow morphologies change significantly (e.g., becoming long, skinny columns in rotating convection [26,27]). In rotating convection, force balances between the inertial, buoyancy, and Coriolis forces lead to distinct emergent phenomena in the rotationally constrained and unconstrained regimes [26]. Scaling laws for heat transport (Nusselt number) and turbulence (Reynolds number) have been theoretically derived and experimentally verified for rotating convection [28–30]. However, the parameter space of magnetoconvection is less well-understood, especially in regimes relevant to astrophysical systems. Laboratory [31–34] and numerical experiments [23,35,36] have studied flow regimes and devised scaling laws for heat transport, but are limited to field strengths that are much smaller than those found in active regions of the Sun. Dynamical regimes of quasistatic magnetoconvection have been quantified by the scaling of heat transport with the buoyancy forcing, the physical structure, and the relative sizes of the forces within the momentum equation [37,38]. The quasistatic approximation assumes the magnetic Reynolds number, R_m , is vanishingly small such that magnetic fluctuations are negligible compared to the external field [39]. However, in many astrophysical environments, e.g., stars, this approximation breaks down due to large magnetic Reynolds number [40]. The regime of nonzero magnetic Reynolds number has been studied frequently in dynamo simulations where the seed magnetic field is weak [41], but it has not been well-studied for the strong-field case.

In this work at finite R_m , we generate and analyze a suite of MHD convection simulations under the Boussinesq approximation. We directly measure the first-order and second-order force balances present in the simulations and define distinct regimes based on leading-order solenoidal force balances. The leading-order balance contains the pressure gradient, and we retrieve the second-order balance by removing the pressure-gradient-like terms to get the solenoidal portions of the forces. Solenoidal forces can be extracted by taking the curl of the momentum equation or projecting the force onto its solenoidal part [42,43]. We largely restrict our studies to 2D to span a wider range of parameter space than would be available in 3D, but we verify our results using select 3D simulations. Our 2D focus allows us to reach Rayleigh (Ra) numbers of 10^{12} and Chandrasekhar

(Q) numbers of 10^{10} , much closer to realistic sunspot values of $O(10^{16})^1$ than previous studies. We study a broad swathe of the Ra - Q parameter space to understand how these input parameters change magnetoconvection regimes.

We measure the degree of magnetic constraint using the ratio of the linear magnetic force (linearized about the strong background field) and nonlinear magnetic force. We identify three regimes in parameter space: a magnetically constrained regime dominated by the linear magnetic force and characterized by highly constrained flows, a magnetically influenced regime where a balance between nonlinear inertial and Lorentz forces emerges, and a transitional regime where the linear and nonlinear Lorentz force are in balance. We find that to simultaneously achieve magnetic constraint and turbulence, simulations require $Q \gtrsim 10^{10}$. We find the output magnetic field strength scales with the Alfvénic Mach number, $M_A \propto \sqrt{\text{Ra}/Q}$, in both regimes. The traditional hydrodynamic flow regime is not achieved at high Ra due to the nonlinear Lorentz force. Despite this, magnetically influenced simulations asymptote to hydrodynamic Nu versus Ra scalings.

This paper is organized as follows. In Sec. II we outline the magnetohydrodynamic equations, numerical methods, and the simulation details. In Sec. III we discuss the dynamical regimes, force balances, and scaling laws. In Sec. IV we discuss the implications of this work and outline future work.

II. EQUATIONS AND METHODOLOGY

We solve the magnetohydrodynamic (MHD) equations nondimensionalized with respect to the freefall velocity,

$$\nabla \cdot \mathbf{u} = 0, \quad (1)$$

$$\frac{\partial \mathbf{u}}{\partial t} + \nabla \varpi + \sqrt{\frac{\text{Pr}}{\text{Ra}}} \nabla \times \boldsymbol{\omega} - T \hat{\mathbf{z}} = \mathbf{u} \times \boldsymbol{\omega} + \frac{1}{M_A^2} \mathbf{J} \times \mathbf{B}, \quad (2)$$

$$\frac{\partial T}{\partial t} - \frac{1}{\sqrt{\text{RaPr}}} \nabla^2 T = -(\mathbf{u} \cdot \nabla) T, \quad (3)$$

$$\nabla \cdot \mathbf{A} = 0, \quad (4)$$

$$\frac{\partial \mathbf{A}}{\partial t} + \nabla \phi + \sqrt{\frac{\text{Pr}}{\text{RaPm}^2}} \mathbf{J} = \mathbf{u} \times \mathbf{B}, \quad (5)$$

where \mathbf{u} is the fluid velocity vector, ϖ is the reduced pressure, \mathbf{B} the magnetic field, \mathbf{A} is the vector potential and satisfies $\mathbf{B} = \nabla \times \mathbf{A}$, $\mathbf{J} = \nabla \times \mathbf{B}$ is the current density, ϕ is the electrostatic potential, T is temperature, and $\boldsymbol{\omega} = \nabla \times \mathbf{u}$ is the vorticity. We impose a background magnetic field $B_0 \hat{\mathbf{z}}$, where B_0 is the strength of the magnetic field. The nondimensional variables Rayleigh number (Ra), magnetic Prandtl number (Pm), Chandrasekhar number (Q), and Prandtl number (Pr) are defined as

$$\text{Ra} \equiv \frac{\alpha g \Delta T L^3}{\nu \kappa}, \quad \text{Pm} \equiv \frac{\nu}{\eta}, \quad Q \equiv \frac{B_0^2 L^2}{\rho \nu \eta \mu_0}, \quad \text{and} \quad \text{Pr} \equiv \frac{\nu}{\kappa}, \quad (6)$$

where α is the thermal expansion coefficient, g is the acceleration due to gravity, ΔT is the temperature difference across the domain, L is the depth of the domain, ν is the viscosity, κ the

¹To estimate the value of Q in a sunspot, we substitute $\mu_0 = 1$ in CGS units and eliminate viscosity in Eq. (6), using Pm to give $Q = \frac{B_0^2 L^2}{(\rho \eta^2)} \text{Pm}$. Using $B_0 = 3000\text{G}$ and $L = 5 \times 10^9 \text{cm}$ from Ref. [44], $\text{Pm} \approx 10^{-5}$ and $\eta \approx 10^6 \text{cm}^2/\text{s}$ from Ref. [45], and $\rho_0 \approx 1.74 \times 10^{-7} \text{g cm}^{-3}$ from Ref. [46], we estimate $Q \approx 1.5 \times 10^{16}$ in a sunspot.

thermal diffusivity, and η the magnetic resistivity. The square Alfvénic Mach number is

$$M_A^2 = \frac{u_{\text{ff}}^2}{v_A^2} = \frac{\text{RaPm}}{Q \text{Pr}}. \quad (7)$$

We hold $\text{Pr} = 0.25$ and $\text{Pm} = 0.5$ fixed such that $\xi = \text{Pr}/\text{Pm} < 1$ causing the onset of convection to be oscillatory, which is the relevant regime for the solar photosphere [47].

A. Force balances and solenoidal forces

To study the primary and secondary force balances, we measure each of the acceleration terms in the momentum equation. Under the Boussinesq approximation, ρ_0 is constant, so acceleration is the same as the forces. Separating the Lorentz term into its linear and nonlinear components, we define the momentum equation in terms of the forces,

$$\frac{\partial \mathbf{u}}{\partial t} + \nabla \varpi = - \underbrace{\sqrt{\frac{\text{Pr}}{\text{Ra}}} \nabla \times \boldsymbol{\omega}}_{\mathbf{f}_v} + \underbrace{T \hat{\mathbf{z}}}_{\mathbf{f}_b} + \underbrace{\frac{1}{M_A^2} \mathbf{J} \times \mathbf{B}_0}_{\mathbf{f}_{\text{ml}}} + \underbrace{\mathbf{u} \times \boldsymbol{\omega}}_{\mathbf{f}_i} + \underbrace{\frac{1}{M_A^2} \mathbf{J} \times \mathbf{B}_1}_{\mathbf{f}_{\text{mn}}}, \quad (8)$$

where \mathbf{f}_v is the viscous force, \mathbf{f}_b is the buoyancy force, \mathbf{f}_{ml} is the linear magnetic force, \mathbf{f}_i is the inertial force, and \mathbf{f}_{mn} is the nonlinear magnetic force. The Lorentz force is split into a linear ($\mathbf{f}_{\text{ml}} = \frac{1}{M_A^2} \mathbf{J} \times \mathbf{B}_0$) and a nonlinear ($\mathbf{f}_{\text{mn}} = \frac{1}{M_A^2} \mathbf{J} \times \mathbf{B}_1$) component, where \mathbf{B}_1 is the perturbation around the background field $\mathbf{B}_0 = 1 \hat{\mathbf{z}}$. The force balances provide insight into the dynamics of the fluid. When convection is constrained by a strong background magnetic field or global rotation, the first-order force balance is expected to be between the constraining force and the pressure gradient. For example, in constrained rotating convection, the primary geostrophic balance is between the Coriolis force and the pressure gradient [26], while for constrained magnetoconvection it is between the magnetic (Lorentz) force and the pressure gradient. In an incompressible flow, any portion of the force that has a divergence must be immediately balanced by pressure to enforce the divergence constraint ($\nabla \cdot \mathbf{u} = 0$). The gradient component of each force only contributes to the pressure gradient, thus is not dynamically relevant [42,43]. By removing this first-order balance involving the pressure gradient, the force balance that directly affects the dynamics can be identified.

In this work, we break these forces up into portions that are solenoidal (divergence-free) and those that are not. Dividing the momentum equation by density allows the forces to be written as acceleration, thus Eq. (8) becomes

$$\partial_t \mathbf{u} + \nabla \varpi = \mathbf{a}_v + \mathbf{a}_b + \mathbf{a}_{\text{ml}} + \mathbf{a}_i + \mathbf{a}_{\text{mn}} = \sum_j \mathbf{a}_j = \sum_j \mathbf{a}_{j,S} + \mathbf{a}_{j,NS}, \quad (9)$$

where we have split $\mathbf{a}_j = \mathbf{a}_{j,S} + \mathbf{a}_{j,NS}$ into its solenoidal ($\mathbf{a}_{j,S}$) and nonsolenoidal ($\mathbf{a}_{j,NS}$) components. Taking the divergence of Eq. (9) gives

$$\partial_t (\nabla \cdot \mathbf{u}) + \nabla^2 \varpi = \sum_j \nabla \cdot \mathbf{a}_{j,S} + \nabla \cdot \mathbf{a}_{j,NS} \Rightarrow \nabla^2 \varpi = \sum_j \nabla \cdot \mathbf{a}_{j,NS}, \quad (10)$$

where we have used the incompressibility constraint ($\nabla \cdot \mathbf{u} = 0$) and that the solenoidal portion of the acceleration is divergenceless ($\nabla \cdot \mathbf{a}_{j,S} = 0$). Thus, Eq. (10) shows that the pressure gradient is composed of the nonsolenoidal portion of the acceleration. Therefore, the solenoidal forces are directly responsible for the acceleration of the fluid,

$$\partial_t \mathbf{u} = \sum_j \mathbf{a}_{j,S}. \quad (11)$$

We decompose the pressure into partial pressures (as in Eq. (4) of Ref. [48]), and remove the pressure gradient portion of each force to retrieve the *solenoidal forces*,

$$\mathbf{a} = -\mathbf{s}_v + \mathbf{s}_b + \mathbf{s}_{ml} + \mathbf{s}_i + \mathbf{s}_{mn}. \quad (12)$$

Equation (12) is the statement that the solenoidal forces are the portions of each force that directly contribute to the fluid acceleration. The solenoidal forces are analogous to the torques in the vorticity equation, because both have the nonsolenoidal portion of the force removed by construction. Since the nonsolenoidal portion can be expressed as a pressure gradient, and the curl of a gradient is zero, the only component left in the vorticity equation is the solenoidal portion. We choose to examine the solenoidal forces in this work because they lack the additional complexity introduced by taking a curl, allowing us to easily disentangle force components aligned with the background field from those which are not. A more detailed comparison between the two methods can be found in Ref. [42]. The nonsolenoidal portion of the forces are not dynamically relevant due to the incompressibility constraint, thus this decomposition only holds for Boussinesq fluids. While it may be possible to decompose the forces in this way for low Mach number compressible flows (e.g., in the anelastic regime where an alternate divergence constant holds), this method does not work when solving the fully compressible continuity equation. See Appendix A for more details on how the solenoidal forces are formed and how they relate to the second-order balance. We output the volume-averaged magnitude of the vector force at each timestep, then report the time-averaged mean once the simulation has reached a steady state. We average over the last half of the simulation by simulation time, which only includes data in the statistically stationary state. We run most simulations for many hundreds of freefall times, so our averages are also taken over many hundreds of freefall times. Due to the computational expense of our most extreme simulations (for $Q = 10^{10}$), that simulation was only evolved for 100 freefall times, so we average over 50 freefall times, and verified by eye that the simulation was in a statistically stationary state and that the computed mean described the data well.

B. Numerics and parameter space

We evolve Eqs. (1)–(5) in time using the pseudospectral code Dedalus [49] using a third-order, four-step, implicit-explicit Runge-Kutta timestepping scheme RK443 [50]. We control our timestep size using both a velocity CFL and a magnetic CFL due to the presence of Alfvén waves which can arise in the nonlinear Lorentz force, details of which can be found in Appendix B. The simulation is bounded above and below by impenetrable, no-slip, fixed temperature, magnetically conducting boundaries. Magnetically conducting boundary conditions require $B_z = J_y = J_x = 0$. In the vector potential formulation setting $A_x = A_y = 0$ will enforce $B_z = 0$. This results in the current density boundary conditions being $J_x = -\partial_x \phi$ and $J_y = -\partial_y \phi$, thus we set $\phi = 0$. The final set of boundary conditions is

$$w = u = T_1 = A_x = A_y = \phi = 0 \text{ at } z = \{0, L_z\}, \quad (13)$$

while the horizontal domain is periodic. Variables are represented as spectral expansions of n_x (and n_y in 3D) horizontal Fourier coefficients and n_z vertical Chebyshev coefficients. To avoid aliasing errors, we use the 3/2 dealiasing rule in all directions. We add random noise temperature perturbations of magnitude 10^{-6} to the background temperature field to start the simulation.

We performed a linear stability analysis using eigentools [51]. The results of this analysis are shown in Fig. 1, where the critical Rayleigh number is $\text{Ra}_{\text{crit}} = \pi^2 Q$. The wave number of the fastest growing linearly unstable convective mode scales as $k_x \propto Q^{1/6}$ for $Q \gg 1$, which is consistent with Refs. [47,52]. This means that the horizontal scale of convection decreases with increasing magnetic field strength and convective cells become narrower [23].

We set the domain aspect ratio $\Gamma = L_x/L_z = 5 \times \frac{2\pi}{k_x}$ (and $L_y/L_z = 5 \times \frac{2\pi}{k_y}$ in 3D), which is five times larger than the onset length scale ($\frac{2\pi}{k_x}$) and so should allow the convection to develop multiple

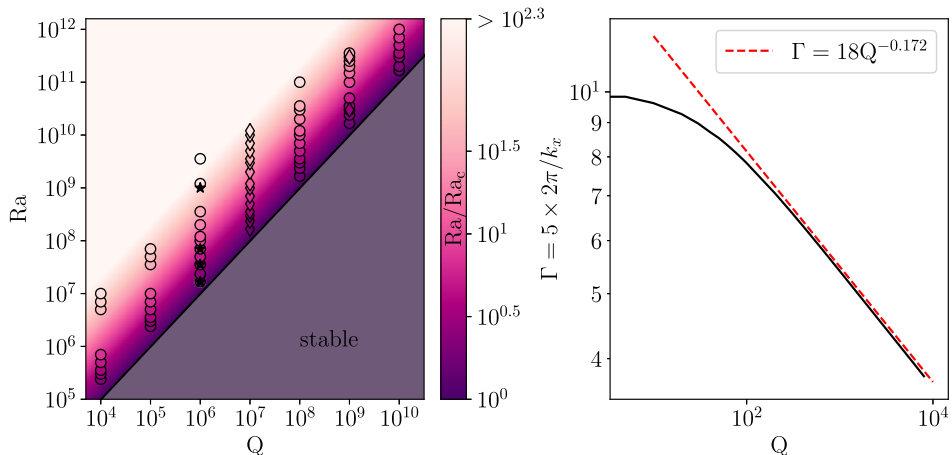


FIG. 1. Plots showing where each simulation lies in parameter space (left) and the aspect ratio dependency on Q (right). Each simulation studied in this work is denoted as a circular marker in the Ra vs Q parameter space, the diamond markers represent simulations shown in Figs. 2 and 4, and starred markers are 3D runs. The line $Ra_c = \pi^2 Q$ is plotted in black; the gray shaded area below the line is linearly stable to convective instabilities. The aspect ratio decreases with Q resulting in tall skinny boxes in the high- Q limit. The red dashed line represents the expected high- Q scaling of $\Gamma \propto Q^{-1/6}$.

structures on its preferred length scale. This is shown in Fig. 1, where the aspect ratio $\Gamma \propto Q^{-1/6}$. We observe the onset of convection is oscillatory, as expected [53].

Figure 1 shows the span of parameter space that we studied. The colorbar denotes the supercriticality of a given (Ra, Q) . Full details of the simulation parameters, resolution, and aspect ratio can be found in Appendix C and the Supplemental Material [54]. Our simulations span from $Ra = 1.2 \times 10^5$ at $Q = 10^4$ to $Ra = 10^{12}$ at $Q = 10^{10}$ in 2D, and we study select 3D runs at $Q = 10^6$ with a Ra range of 1.2×10^7 to 10^9 . The scripts used to run these simulations are publicly available at [55].

III. RESULTS

A. Dynamical regimes

Figure 2 shows the vertical magnetic field in different dynamical regimes for both 2D (top) and 3D (bottom) simulations. The left visualizations are from simulations where the Rayleigh number is just above critical, thus the convective plumes follow the vertical background magnetic field lines with no deviation or turbulence. As the Rayleigh number is increased the system becomes more turbulent and less constrained by the background field, smaller scales emerge, and the magnetic field concentrates along upflows and downflows. This is seen in the right-hand-side visualizations where the high-supercriticality convective driving is sufficient to sweep the field lines to the convective cell boundaries. Boussinesq systems exhibit an up-down symmetry, which means the pattern of convective cells at the top and bottom boundaries are complementary [23]. Strong regions of positive vertical magnetic field are found in the plume launching sites (hot regions on the lower boundary or cold regions on the upper boundary). As these plumes buoyantly rise or fall, the magnetic field becomes less intense and changes sign before impacting on the far boundary.

In nature, convective flows can be simultaneously highly magnetically constrained and more turbulent than those shown on the left side of Fig. 2, so our goal is to determine where in parameter space simulations are *both* constrained and turbulent. We measure the degree of magnetic constraint using the ratio of the linear magnetic force \mathbf{f}_{ml} and the nonlinear magnetic force \mathbf{f}_{mn} . When the

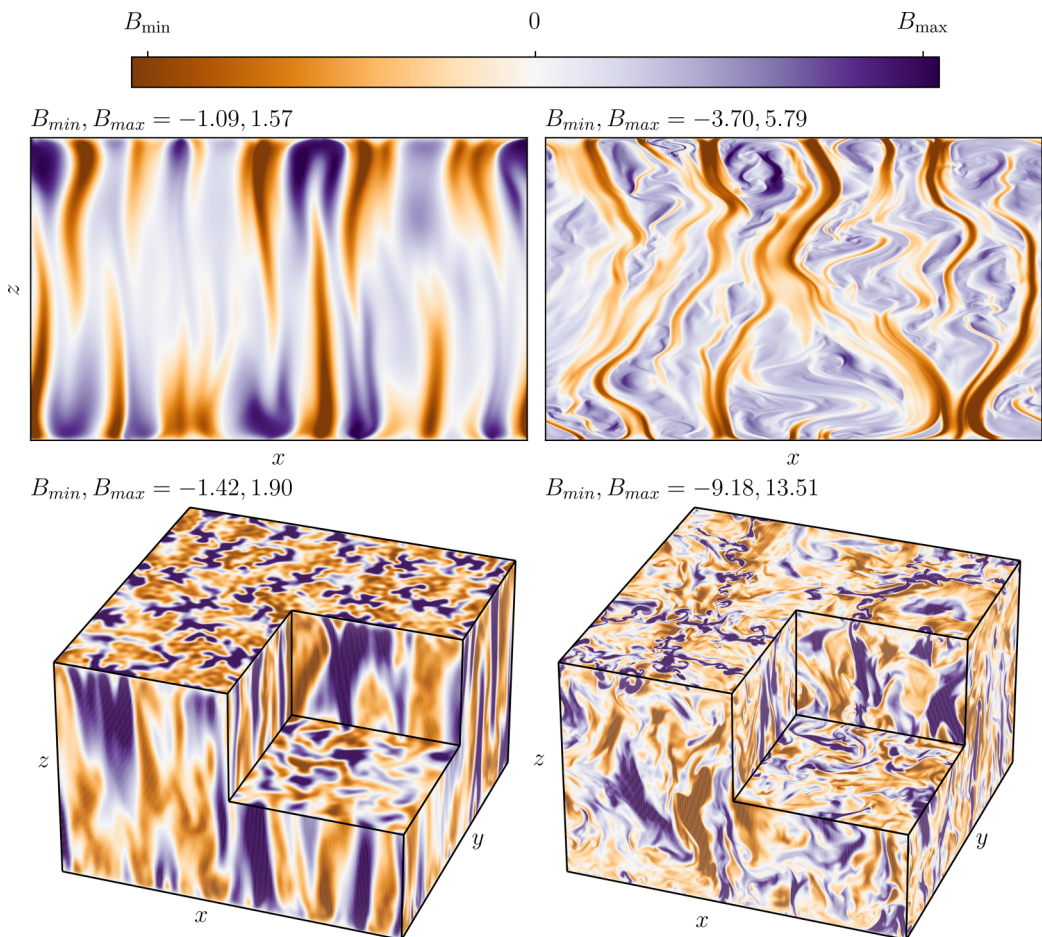


FIG. 2. The vertical component of the full magnetic field ($\mathbf{B}_0 + \mathbf{B}_1$) is visualized for select 2D (top) and 3D (bottom) simulations. The 2D simulations are at $Q = 10^9$ with $Ra = 3 \times 10^{10}$ (left) and $Ra = 3.55 \times 10^{11}$ (right). The 3D simulations are at $Q = 10^6$ with $Ra = 3 \times 10^7$ (left) and $Ra = 10^9$ (right). The characteristic magnetic Reynolds numbers Rm of the simulations are as follows: 3730.4 (top left), 21065.5 (top right), 131.6 (bottom left), and 2641.6 (bottom right). As the Rayleigh number increases, flows become more turbulent and degree of constraint decreases. At low supercriticality (left), magnetic field lines and flows are columnated along the background field. At high supercriticality (right), the magnetic field lines are swept and concentrated by the flow.

linear Lorentz force is dominant ($\mathbf{f}_{ml} > \mathbf{f}_{mn}$), the flow is constrained to follow the field lines (Fig. 2, left) thus we call this regime the *constrained* regime. When the nonlinear Lorentz force dominates ($\mathbf{f}_{mn} > \mathbf{f}_{ml}$), depicted on the right of Fig. 2, the system is not constrained but exhibits turbulent flow that is distinctly different from hydrodynamical Rayleigh-Bernard convection (RBC). Thus, we call this regime *magnetically influenced*, because magnetic nonlinearities appreciably influence the observed dynamics. We measured the ratio of the vertical velocity and the horizontal velocity $\langle \mathbf{w} \rangle / \langle \mathbf{u} \rangle$ in the bulk for both regimes. We found that the average ratio was approximately an order of magnitude higher in the constrained regime (Fig. 2, left) where it was 98.4, than in the magnetically influenced regime (Fig. 2, right) where it was 18.2, indicating that more of the flow is in the direction of the imposed field in the constrained regime. We measured the average angle between the velocity vectors, $\tan^{-1}(|\mathbf{u}|/|\mathbf{w}|)$ in the bulk for the constrained and magnetically

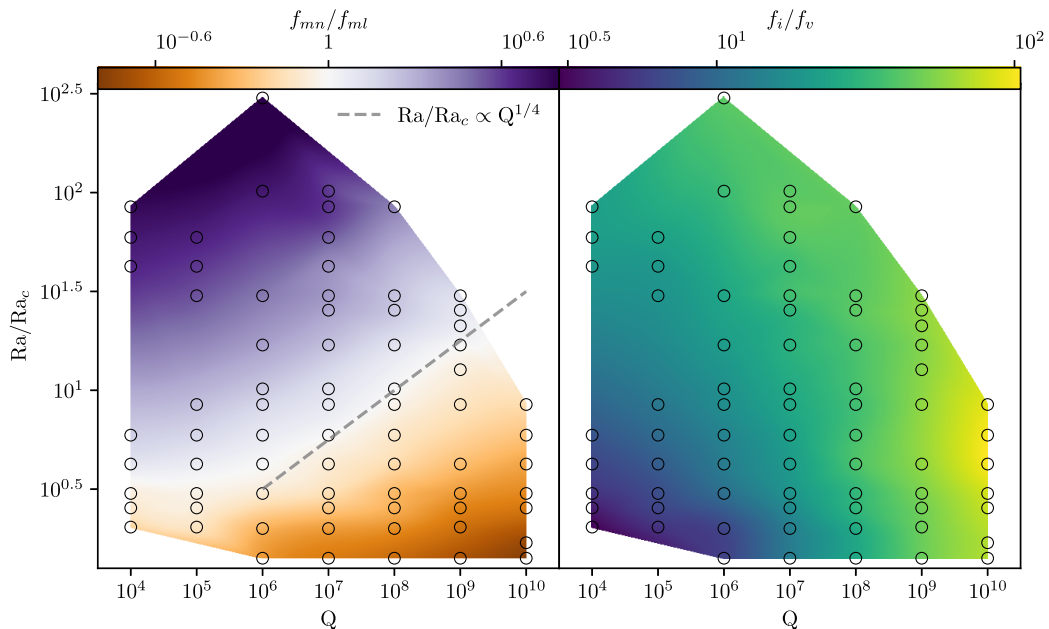


FIG. 3. Parameter space maps of supercriticality vs Q where color denotes (left) the ratio of the linear magnetic force to the nonlinear magnetic force, and (right) the ratio of the inertial force to the viscous force. The circles are simulation data and the background color is an interpolation of the data. As Q increases the range of supercriticality for which the system is magnetically constrained (orange, left) increases in size. Furthermore, as Q increases, simulations become turbulent (yellow, right) at a lower supercriticality.

influenced regimes. In the constrained regime, the average angle was closer to 0° inclination from the vertical, and thus more aligned with the imposed field than the magnetically influenced regime.

We find that the transition from the constrained to magnetically influenced regime depends on both the Chandrasekhar number, Q , and the Rayleigh number, Ra . Figure 3 demonstrates that the range of supercriticalities for which a simulation is magnetically constrained increases with the Chandrasekhar number, Q . The color scale represents the degree of magnetic constraint, $\mathbf{f}_{mn}/\mathbf{f}_{ml}$ (left plot) with the orange band being constrained (\mathbf{f}_{ml} dominates) and the purple band being magnetically influenced (\mathbf{f}_{mn} dominates). The white band represents simulations where $\mathbf{f}_{ml} \sim \mathbf{f}_{mn}$, i.e., the transition point between the regimes. We see a clear trend where the supercriticality at which a simulation transitions from constrained (orange) to influenced (purple) increases with Q . The supercriticality at which the transition occurs increases with Q is given by $Ra/Ra_c = 0.1Q^{1/4}$, shown by the gray dashed line in Fig. 3.

Interestingly, the simulations in the far right of the orange band are also relatively turbulent. This is shown on the right-hand-side plot, where the color bar represents the ratio of the inertial force \mathbf{f}_i and the viscous force \mathbf{f}_v , which is a direct measure of the Reynolds number. Yellow regions of this plot are turbulent and blue regions are laminar. The Reynolds number increases both with increasing supercriticality and increasing Q ; the highest Reynolds number simulation in our study coincides with the magnetically constrained regime at $Q = 10^{10}$ and $Ra/Ra_c \approx 5$. At this supercriticality for smaller Q , the convection is no longer constrained or turbulent. Convection can be achieved at a large Q and moderate supercriticality. Therefore, if it were possible to simulate values of Q comparable to those in sunspots (where $Q \approx 10^{16}$), there would be a turbulent constrained regime. This plot also shows that supercriticality is not a good measure of constraint, because the regime transition does not stay constant as Q increases. The high Re flows at large Q look quite different from those in turbulent hydrodynamical RBC, because the ohmic dissipation strongly laminarizes the flow. While

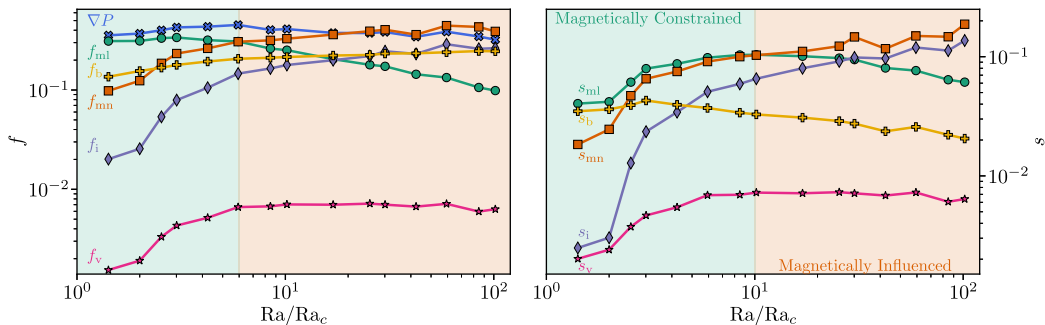


FIG. 4. Shown are the volume-averaged magnitudes of the full forces (left) and the solenoidal portions of the forces (right) as a function of the supercriticality for $Q = 10^7$. The pressure gradient (blue crosses, left) balances the linear magnetic force (green circles) at low supercriticality and the nonlinear magnetic force (orange squares) at higher supercriticalities. For the solenoidal forces (right), at low supercriticality, the linear magnetic force (green circle) balances the buoyancy force (yellow crosses). The nonlinear magnetic force (orange square) and inertial force (purple diamonds) increase with increasing supercriticality. At high supercriticalities a balance between the nonlinear magnetic force and the inertial force occurs. The color change from green to orange shows the point where the nonlinear Lorentz force becomes dominant.

plumes are not strictly confined to the field lines, they are still guided along the vertical field, and there are no small scale vortices (e.g., Ref. [56], Fig. 2).

B. Force balances

We demonstrated in Figs. 2 and 3 that increasing Ra at constant Q changes the leading force balance and thus the system's magnetic constraint or turbulence. We examine the solenoidal force balances as a function of supercriticality at $Q = 10^7$ in Fig. 4, which shows the volume averaged value of the inertial (purple diamonds), nonlinear magnetic (orange squares), linear magnetic (green circles), viscous (pink stars), and buoyancy (yellow crosses) forces for both the full forces (left) and the solenoidal forces (right). The full force plot also includes the pressure gradient (blue crosses) to demonstrate the first-order balances. The pressure gradient is always balanced by the Lorentz force, with the first-order balance being the linear portion in the magnetically constrained regime and the nonlinear portion in the magnetically influenced regime. Focusing on the right plot, at low supercriticality, the solenoidal portion of the linear magnetic force (green circles) dominates and is initially in balance with the buoyancy solenoidal force (yellow crosses). At supercriticalities $Ra/Ra_c \gtrsim 10$, shown by the orange shaded region in Fig. 4, the nonlinear magnetic force dominates and comes into balance with the inertial (purple diamonds) force. The green shaded region where the linear magnetic solenoidal force dominates is the magnetically constrained regime, while the orange shaded region is where the nonlinear magnetic solenoidal force dominates and is the magnetically influenced regime. There is also a transitional regime where all the forces (other than viscous) are roughly in balance. At the highest supercriticality, we observe the force balance $\mathbf{s}_{mn} \approx \mathbf{s}_i > \mathbf{s}_b$, which is very different from $\mathbf{s}_b \approx \mathbf{s}_i$ in standard bulk dynamics in Rayleigh Bérnard convection (RBC). Even when it is not constrained by the background field, the nonlinear nature of magnetoconvection is fundamentally different from hydrodynamical RBC. The nonlinear feedback between the inertial and Lorentz forces causes this, and this may be reminiscent of dynamo action, though we note that dynamos cannot occur in 2D or even in 3D when you have a DC field [15]. The presence of this fully nonlinear force balance is why we refer to this regime as “magnetically influenced” and not “magnetically unconstrained,” because magnetism is still very much important even if the initial background field does not dominate the dynamics. We find that the trend with increasing Ra changes more drastically for f_{ml} than other forces when comparing the full forces

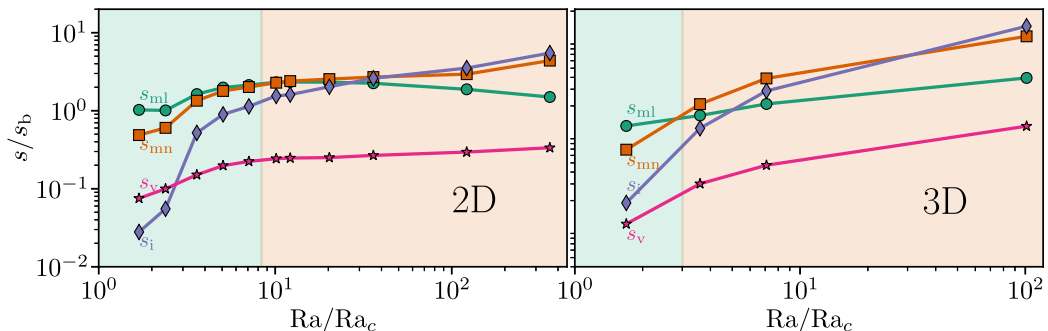


FIG. 5. Shown are the volume-averaged magnitudes of the solenoidal portions of the forces normalized by the magnitude of the solenoidal buoyancy force as a function of the supercriticality at $Q = 10^6$ for both 2D (left) and 3D (right). The supercriticality at which the transition from constrained to magnetically influenced occurs is lower in 3D, and the linear Lorentz force increases in magnitude less steeply.

(Fig. 4, left) versus the solenoidal forces (right), and suspect this is due to its large contribution to the pressure gradient. Interestingly, the transition from the constrained regime appears to occur at $Ra/Ra_c \gtrsim 6$ when using the full forces, which is slightly lower than in the solenoidal forces.

We ran select three-dimensional simulations at $Q = 10^6$ for comparison with our 2D results. We compare the solenoidal force balance from 2D (left) and 3D (right) simulations in Fig 5. We find the same pattern in 2D and 3D; the linear magnetic force dominates for low supercriticality with flow structures being laminar and constrained, and as supercriticality is increased the nonlinear force becomes dominant, and flow structures become more turbulent. The transition between these regimes occurs at lower supercriticality in 3D than in 2D. The nonlinear Lorentz (orange squares) and inertial (purple diamonds) forces behave similarly both in 2D and 3D, however the linear Lorentz force increases in magnitude less steeply in 3D than in 2D. The linear Lorentz force is a measure of horizontal currents, and this discrepancy may be due to the different morphology of current sheets surrounding the upflows and downflows (regions of strong B_z) in 3D (where they are arbitrary two-dimensional manifolds) than in 2D (where they are planes). While the forces appear to behave in a similar manner, we acknowledge that RBC differs in 2D and 3D, especially scaling laws [57], and thus we focus our remaining discussion on the 2D cases.

The change in the dominant force from linear magnetic to nonlinear magnetic can be explained using dimensional analysis. Just above onset the system is very constrained, therefore the linear magnetic force dominates. This is because the linear magnetic force scales as

$$\mathbf{s}_{ml} = \frac{1}{M_A^2} \mathbf{J} \times \hat{\mathbf{z}} = \frac{1}{M_A^2} (\nabla \times \mathbf{B}) \times \hat{\mathbf{z}} \approx \frac{1}{M_A^2} \frac{B}{l}. \quad (14)$$

Conversely, the nonlinear magnetic force scales as

$$\mathbf{s}_{mn} = \frac{1}{M_A^2} \mathbf{J} \times \mathbf{B} = \frac{1}{M_A^2} (\nabla \times \mathbf{B}) \times \mathbf{B} \approx \frac{1}{M_A^2} \frac{B^2}{l}, \quad (15)$$

which differs from the linear magnetic force by a factor of B . When the magnetic field fluctuations are smaller than 1 (the nondimensional magnitude of the background field), as is the case when the system is constrained, then $\mathbf{s}_{mn}/\mathbf{s}_{ml} \sim B < 1$. As Ra is increased, the degree of constraint decreases, and the system transitions from being constrained to being magnetically influenced because $B \gtrsim 1$.

Examining the solenoidal force balances across the whole parameter space allows different regimes to be identified. While Fig. 4 shows how the solenoidal force balances change for fixed Q , Fig. 6 shows the solenoidal force balances change for all values of Q . Shown are the linear (left) and nonlinear (right) magnetic solenoidal forces versus the buoyancy solenoidal force, both normalized

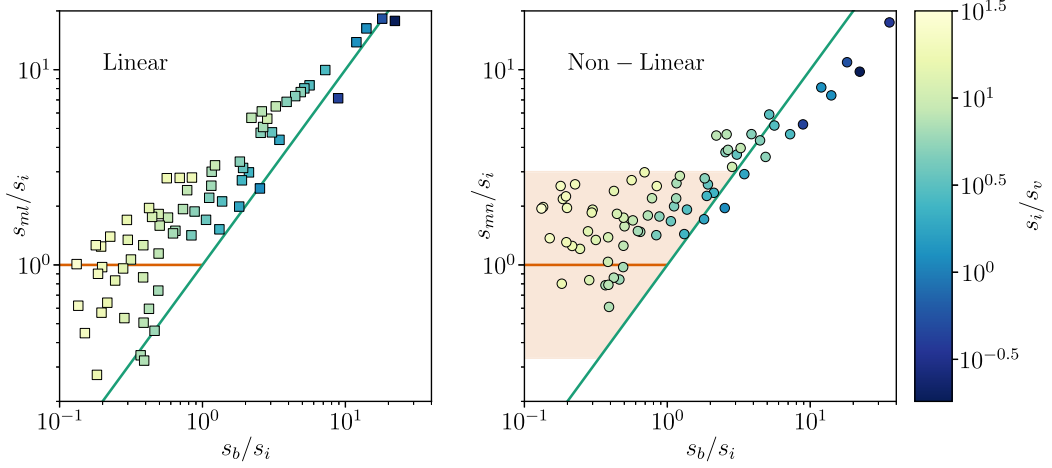


FIG. 6. Shown is the solenoidal force balance parameter space, depicting how the solenoidal linear magnetic force \mathbf{s}_{ml} (left) and solenoidal nonlinear magnetic force \mathbf{s}_{mn} (right) scale vs the solenoidal buoyancy force \mathbf{s}_b ; both axes are normalized by the solenoidal inertial force \mathbf{s}_i . The color scale shows the solenoidal Reynolds number where the yellow points are more turbulent, such that blue points are in the constrained regime while yellow points are in the magnetically influenced regime. The green line shows where $s_m = s_b$, the orange line shows where $s_m = s_i$, and the orange band shows where $s_{mn} \approx s_i$.

by the inertial solenoidal force. The color denotes the solenoidal Reynolds number ($\mathbf{s}_i/\mathbf{s}_v$), which is a measure of turbulence, where the yellower points are more turbulent. The color scale here shows a maximum value of the solenoidal Reynolds number to be $10^{1.5}$, which is orders of magnitude lower than the traditionally measured bulk Reynolds number (uL/ν) as seen in Fig. 7 (right). This also explains why the flow dynamics appear more laminar compared to turbulent RBC at similar traditional Re values.

In Fig. 6 the green line shows where the magnetic force (\mathbf{s}_m) balances the buoyancy force (\mathbf{s}_b). The top right corner of each plot is where the laminar magnetically constrained regime lies. In this regime, the linear magnetic force (left plot) balance follows this relationship closely allowing the following force balance to be defined,

$$\frac{\mathbf{s}_{ml}}{\mathbf{s}_i} \approx \frac{\mathbf{s}_b}{\mathbf{s}_i} \longrightarrow \mathbf{s}_{ml} \approx \mathbf{s}_b \gg \mathbf{s}_i, \quad (16)$$

the linear magnetic force balances the buoyancy force, and inertial forces are small.

The orange horizontal line shows where the magnetic force equals the inertial force. The linear Lorentz force (left) continues to roughly balance the buoyancy force (green line) even as simulations transition to the magnetically constrained regime and become more turbulent (yellow). The inertial force now becomes large in this regime, especially for large Q ; instead of scaling with the buoyancy force, the nonlinear magnetic force (right) comes into balance with the inertial force which corresponds to the population of simulations in the orange band on the right-hand plot. Since Ra must be large to overcome the linear Lorentz force for high Q , this results in the inertial force being large once the system transitions to the magnetically influenced regime. In Fig. 6 it can be seen that the nonlinear magnetic force (right, circles) is larger than the linear magnetic force (left, squares) with $\mathbf{s}_{mn}/\mathbf{s}_i \approx 1$ and $\mathbf{s}_{mn} > \mathbf{s}_b$. Therefore, in the magnetically influenced regime the force balance is

$$\mathbf{s}_{mn} \approx \mathbf{s}_i > \mathbf{s}_b, \quad (17)$$

which is quite different from the expected hydrodynamical balance $\mathbf{s}_b \approx \mathbf{s}_i$. This is also shown in Fig. 4 for one Q , while in Fig. 6 it is shown for a full suite at many different Q 's.

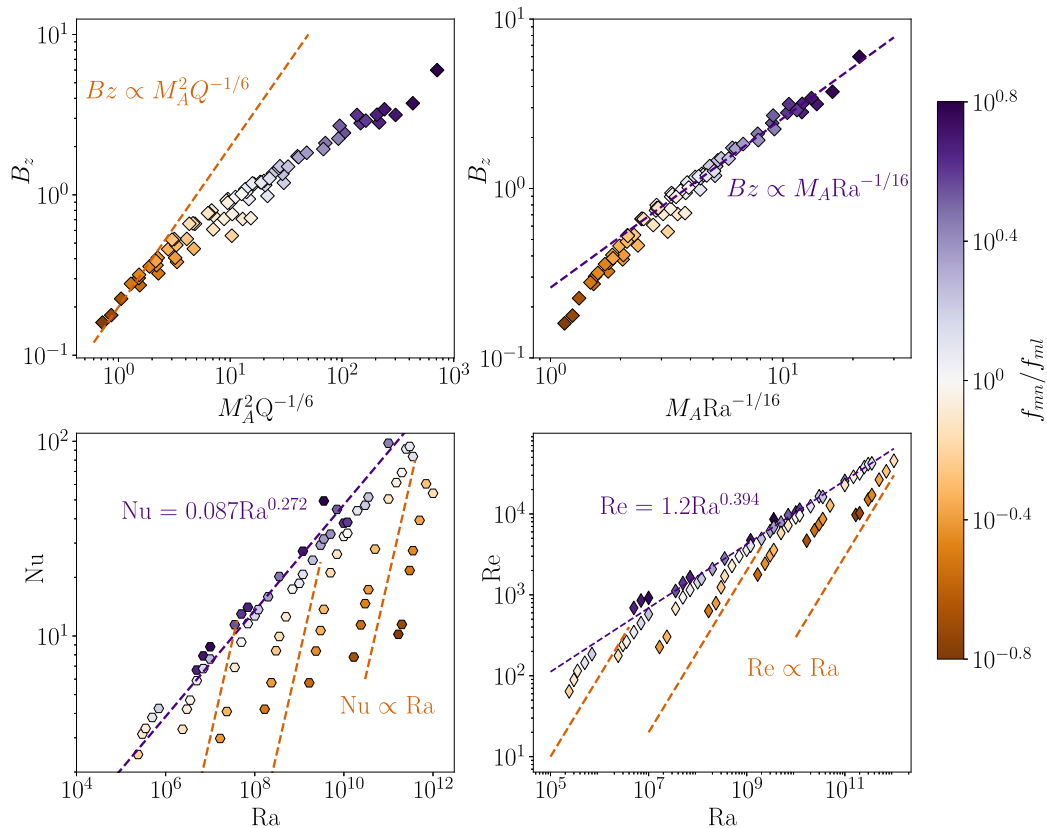


FIG. 7. Scalings derived for the vertical magnetic field B_z (top), the efficiency of heat transport Nusselt number Nu (bottom, left), and the Reynolds number Re (bottom, right). The constrained systems (orange) are characterized by a scaling of $B_z \propto M_A^2 Q^{1/6}$ (top, left), $Nu \propto Ra$, and $Re \propto Ra$, both shown by the orange dashed lines. As simulations become magnetically influenced (purple), they follow the classical RBC scaling where the magnetic field scales as $B_z \propto M_A Ra^{-1/16}$ (top, right), $Nu \propto Ra^{2/7}$, and have a Reynolds number scaling of $Re = 1.42 Ra^{0.386}$.

There does exist a regime where all four forces are roughly in balance. Here, $\mathbf{s}_{mn} \approx \mathbf{s}_{ml} \approx \mathbf{s}_i \approx \mathbf{s}_b$, and we call this regime the transitional regime. This is reminiscent of—but still different from—the coriolis-archimedian-inertial (CAI) triple balance seen in rotationally constrained convection where $\mathbf{s}_i \approx \mathbf{s}_b \approx \mathbf{s}_c$ (where \mathbf{s}_c is the coriolis force [26]), the difference is due to the presence of the dominant nonlinear magnetic force. The description of force balances in transitional regimes remains challenging even for rotationally constrained convection [26]; deducing the proper scaling laws within this regime is beyond the scope of this work.

C. Scaling laws

Since the solenoidal forces describe the acceleration felt by the fluid, the previously defined balances can be used to find how parameters scale in each regime. Taking the balance defined in Eq. (16) we perform dimensional analysis which gives us an estimate for the relationship between input parameters and the evolved variables.

We expect strong-field magnetoconvection to behave like rapidly rotating convection where an unstable mean temperature gradient is sustained [see, e.g., Eq. (26) of Ref. [26]]. However, in our simulations we find that the bulk fluid is generally isothermized by the convection, so we

approximate the buoyancy force as

$$\mathbf{s}_b = T_1 \approx 1, \quad (18)$$

where we assume the temperature fluctuations have a magnitude $T_1 \approx 1$ which is the nondimensional temperature difference between our fixed temperature boundary conditions. Substituting this and the definition of the linear magnetic force [Eq. (14)] into Eq. (16) gives

$$\mathbf{s}_{ml} = \frac{1}{M_A^2} \frac{B}{l} = T_1 = \mathbf{s}_b \approx 1 \Rightarrow B \approx M_A^2 l, \quad (19)$$

meaning the magnetic field fluctuations scale with the Alfvénic Mach number multiplied by the representative length scale. We measured a length scale using $|\mathbf{u}|/|\boldsymbol{\omega}|$ in the bulk of our magnetically constrained regime domains and found that $\ell \approx 0.3Q^{-1/6} \frac{Ra}{Ra_c}^{-1/4}$ describes our simulation data well, so in the small supercriticality limit where flows are strongly constrained the $Q^{-1/6}$ approximation here is valid. Assuming $l \propto Q^{-1/6}$, we arrive at

$$B \approx M_A^2 Q^{-1/6} \quad (20)$$

for the magnetically constrained regime. In Fig. 7 (top left) we show the scaling for the vertical magnetic field B_z in the magnetically constrained regime. The color bar shows the ratio of the nonlinear magnetic force to the linear magnetic force with yellow points being in the constrained regime and purple points being in the magnetically influenced regime. We see that the derived relationship holds well for strongly constrained points, but soon deviates as the system becomes less constrained. This is expected, as the linear magnetic force and buoyancy force are only truly in balance for very low supercriticality as seen in Fig. 6.

In the magnetically influenced regime, we take Eq. (17) and again perform dimensional analysis using the definition for the nonlinear magnetic force defined in Eq. (15),

$$\mathbf{s}_i \approx \mathbf{s}_{mn} \Rightarrow \frac{u^2}{l} \approx \frac{1}{M_A^2} \frac{B^2}{l} \Rightarrow B \approx \sqrt{u M_A^2}, \quad (21)$$

which implies that the magnetic field sets the velocity magnitude. To find how the velocity scales, we assume a balance between magnetic resistivity and induction. We balance the solenoidal terms in the induction equation [Eq. (5)],

$$\sqrt{\frac{Pr}{RaPm^2}} \mathbf{J} \approx \mathbf{u} \times \mathbf{B}. \quad (22)$$

Using dimensional analysis on the current gives

$$\sqrt{\frac{Pr}{RaPm^2}} \frac{\mathbf{B}}{\ell} \approx |\mathbf{u}| |\mathbf{B}| \Rightarrow u \approx \frac{1}{\ell} \sqrt{\frac{Pr}{RaPm^2}}. \quad (23)$$

Empirically, we measure $\ell \propto Ra^{-3/8}$ in the magnetically influenced regime. We see that the turbulent length scale of flows follows a different scaling than the onset scaling, as in rotating convection [58], but a detailed derivation of this length scale is beyond the scope of the present study. Thus, at fixed Pr and Pm we find the velocity scales as $u \approx Ra^{-1/8}$. Substituting this into Eq. (21), we find

$$B_z \approx M_A Ra^{-1/16} \quad (24)$$

for the magnetically influenced regime. This scaling is shown in Fig. 7 (top right) where we find the magnetically influenced points (purple) fit the derived relationship well.

The efficiency of convection is typically measured by the Nusselt number (Nu),

$$Nu = 1 + (Ra Pr)^{1/2} \left\langle \frac{wT}{\langle -\Delta T \rangle} \right\rangle, \quad (25)$$

TABLE I. Table containing scaling equations for each Q in the magnetically constrained regimes.

Q	αNu^γ	βRe^χ
10^6	$\alpha = 1.1 \times 10^{-8} \gamma = 1.17$	$\beta = 2.29 \times 10^{-10} \chi = 1.65$
10^7	$\alpha = 5.54 \times 10^{-8} \gamma = 0.962$	$\beta = 4.95 \times 10^{-8} \chi = 1.23$
10^8	$\alpha = 1.68 \times 10^{-9} \gamma = 1.17$	$\beta = 1.07 \times 10^{-6} \chi = 1.00$
10^9	$\alpha = 4.15 \times 10^{-10} \gamma = 1.04$	$\beta = 2.38 \times 10^{-6} \chi = 0.91$
10^{10}	$\alpha = 1.04 \times 10^{-8} \gamma = 0.815$	$\beta = 8.41 \times 10^{-7} \chi = 0.895$

where $T = T_0 + T_1$ and $\langle \cdot \rangle$ represents a volume average. Convective efficiency is determined by where in the domain (boundary or bulk) the thermal and viscous energy is dissipated [57]. We plot Nu versus Ra in Fig. 7 (bottom left) where the color scale shows the degree of constraint in the system according to the ratio of the nonlinear to linear portions of the Lorentz force. We find that in the magnetically constrained regime (orange points), Nu increases rapidly with increasing supercriticality and has a $\text{Nu} \propto \text{Ra}$ dependency, shown by the orange dashed lines. Table I shows scaling exponents for Nu and Re for each Q in the magnetically constrained regime. Numerical simulations in the quasistatic regime by Yan *et al.* [37] and scaling law arguments presented by Plumbley and Julien [29] also confirm this $\text{Nu} \propto \text{Ra}$ in regimes with large Q and low supercriticality. Interestingly, once the nonlinear magnetic force strongly dominates, the classical RBC scaling of $\text{Nu} \propto \text{Ra}^{2/7}$ emerges. A fit to Nu versus Ra for simulations with $f_{\text{mn}}/f_{\text{ml}} \geq \sqrt{2}$ yields $\text{Nu} = (0.087 \pm 0.04)\text{Ra}^{0.272 \pm 0.008}$. We choose these simulations as this corresponds to a fluctuating magnetic field energy that is two times greater than the background magnetic field energy, meaning these simulations sit comfortably in the magnetically influenced regime. As shown in Figs. 4 and 6, the magnetically influenced regime (purple points) have a very different force balance to that of traditional RBC. Despite this, these points follow the same scaling as hydrodynamical RBC. Yan *et al.* [37] also finds that Nu tends to this scaling for the most turbulent of the simulations in their parameter suite. A similar result was found by Julien *et al.* [59] for turbulent rapidly rotating systems, where an increase in Ra lead to a scaling of $\text{Nu} = (0.144 \pm 0.006)\text{Ra}^{0.288 \pm 0.003}$, the larger prefactor is due to a difference in Pr. At higher Ra these constrained rapidly rotating systems transition to turbulence and behave much like the magnetically influenced regime we have discussed. The emergence of the hydrodynamic RBC scaling suggests that heat transport is dominated in the boundary layer by sheared regions between plume sites [60,61].

We show how the traditional Reynolds number, $\text{Re} = \sqrt{\text{Ra}/\text{Pr}}|\mathbf{u}|$, scales with Ra in Fig. 7 (bottom right). We find that Re in the magnetically constrained regime (orange points) increases rapidly with Ra resulting in a $\text{Re} \propto \text{Ra}$ scaling law. In the magnetically influenced regime (purple points) we find the scaling law $\text{Re} = (1.42 \pm 0.027)\text{Re}^{0.386 \pm 0.008}$. This is consistent with our measured velocity scaling as substituting $u \approx \text{Ra}^{-1/8}$ into $\text{Re} = u\sqrt{\text{Ra}/\text{Pr}}$ gives $\text{Re} \propto \text{Ra}^{-3/8}$.

IV. DISCUSSION AND FUTURE WORK

In this work, we present and analyze a suite of 2D and 3D simulations of strong-field, Rayleigh-Bénard magnetoconvection. Our 2D suite extends to a state-of-the-art value of $Q = 10^{10}$; for comparison, previous 3D simulations have achieved a maximal $Q = 10^8$ under the quasistatic approximation [37] and $Q = 10^6$ with nonlinear Lorentz forces [23]. The contributing forces in the momentum equation were measured directly. We derived and solved equations for the solenoidal forces, which allowed us to directly measure the acceleration that is felt by the fluid. We demonstrated that at low supercriticality the flow is laminar and dominated by the linear magnetic force, which is in balance with the buoyancy force. As supercriticality is increased the dominant force balance changes, with the inertial and nonlinear magnetic force both becoming dynamically important. We find a similar result in 3D, with the exception that the transition from constrained

to magnetically influenced occurs at a lower supercriticality. We directly measure the degree of constraint on the system as determined by the ratio of the linear magnetic force and the nonlinear magnetic force. The range of supercriticalities for which the constrained regime exists increases with Q . Thus, as Q approaches larger values, there exists a regime where the flow is constrained but also turbulent. We categorized three regimes based on the leading-order solenoidal force balance:

(1) The constrained regime characterized by laminar flows following the field lines, where the linear magnetic force and the buoyancy force are in balance $\mathbf{s}_{ml} \approx \mathbf{s}_b$.

(2) The transitional regime which is the most dynamically interesting with constrained yet turbulent convection, where the force balance is a complicated relationship between all nonviscous forces $\mathbf{s}_{ml} \approx \mathbf{s}_{mn} \approx \mathbf{s}_i \approx \mathbf{s}_b$.

(3) The magnetically influenced regime which is reminiscent of hydrodynamical RBC but displays different dynamics due to the large nonlinear Lorentz force balancing the inertial force $\mathbf{s}_{mn} \approx \mathbf{s}_i$.

We argue that this differs greatly from the analogous problem of rotational convection described in, e.g., Ref. [26] due to the nonlinear magnetic force remaining dominant even as the system becomes turbulent. A similar result has been found under QSA where extremely large Rayleigh numbers would be required for the Lorentz force to play a negligible role [37]. Future work should further explore appropriate scaling laws to characterize this regime.

In the magnetically constrained regime, the magnetic field fluctuations scale as $B \propto M_A^2 Q^{-1/6}$, while in the magnetically influenced regime they scale roughly as $B \propto \sqrt{M_A^2 Q^{-1/6}}$. In the constrained regime, the Nusselt number increases as $\text{Nu} \propto \text{Ra}$, consistent with previous work [29,37]. In the magnetically constrained regime, a classical hydrodynamic scaling of $\text{Nu} \propto \text{Ra}^{2/7}$ is seen, despite drastically different dynamics from RBC. The derived scaling laws work well for the constrained regime, but the magnetically influenced regime requires a deeper theoretical exploration, which is beyond the scope of this work.

This work demonstrates the challenge of simulating regimes found in magnetically constrained astrophysical systems. We have shown that strong-field magnetoconvection is not analogous to rotating convection when the quasistatic approximation is relaxed. We do not find a regime in our simulations which resembles hydrodynamical RBC due to the dominance of the nonlinear Lorentz force. While we simulated high Q regimes, we were still orders of magnitude away from those in the most magnetized solar environments like sunspots. While many open questions remain, our results suggest that state-of-the-art simulations at high- Q and moderate supercriticality should reproduce the constrained-but-turbulent regime of natural environments like sunspots.

ACKNOWLEDGMENTS

This work was supported by NASA HTMS Grant No. 80NSSC20K1280 and NASA SSW Grant No. 80NSSC19K0026. I.C. was additionally supported by the George Ellery Hale Graduate Fellowship in Solar, Stellar, and Space Physics at University of Colorado. E.H.A. is funded as a CIERA Postdoctoral fellow and thanks CIERA and Northwestern University. Computations were conducted with support by the NASA High End Computing (HEC) Program through the NASA Advanced Supercomputing (NAS) Division at Ames Research Center on Pleiades with allocation GIDs s1647 and s2114. We thank A. Fraser and K. Julien for helpful discussions. We also thank the two anonymous referees for their detailed feedback which greatly improved this manuscript.

APPENDIX A: DERIVATION OF SOLENOIDAL FORCES

As discussed in Sec. II, solenoidal forces are the divergence free portion of forces and contribute directly to the fluid acceleration. It can be shown that the pressure gradient is set by the nonsolenoidal forces. Dividing the momentum equation by density allows the forces to be written as

accelerations. Acceleration can be decomposed into the solenoidal and nonsolenoidal components,

$$\vec{a} = \vec{a}_S + \vec{a}_{NS}. \quad (\text{A1})$$

Taking the divergence gives

$$\nabla \cdot \vec{a} = \nabla \cdot \vec{a}_S + \nabla \cdot \vec{a}_{NS} = \nabla \cdot \vec{a}_{NS}, \quad (\text{A2})$$

since, by definition, $\nabla \cdot \vec{a}_S = 0$. Equation (8) can be written as

$$\partial_i \vec{u} + \nabla \varpi = \sum_i \vec{a}_i. \quad (\text{A3})$$

Taking the divergence of this, knowing that the fluid is incompressible ($\nabla \cdot \mathbf{u} = 0$) gives

$$\nabla^2 \varpi = \sum_i \nabla \cdot \vec{a}_i, \quad (\text{A4})$$

which, due to Eq. (A2), gives

$$\nabla^2 \varpi = \sum_i \nabla \cdot \vec{a}_{i,NS}. \quad (\text{A5})$$

This means that the pressure gradient is set by the nonsolenoidal part of the acceleration. Thus,

$$\partial_i \vec{u} = \sum_i \vec{a}_{i,S}, \quad (\text{A6})$$

the solenoidal forces are equal to the acceleration of the fluid and directly control the dynamics.

Equation (A5) can be decomposed into a partial pressure for each force i ,

$$\nabla^2 \varpi_i = \nabla \cdot \vec{a}_{i,NS}, \quad (\text{A7})$$

which when solved with impenetrable, no-slip, fixed temperature, magnetically conducting boundary conditions,

$$\mathbf{f}_i = \partial_z \varpi_i \quad \text{at} \quad z = \{0, L_z\} \quad (\text{A8})$$

gives \vec{a}_{NS} for each force.

The total acceleration \vec{a} is measured directly, so subtracting the nonsolenoidal acceleration \vec{a}_{NS} gives

$$\vec{a}_S = \vec{a} - \vec{a}_{NS}. \quad (\text{A9})$$

APPENDIX B: DERIVATION OF MAGNETIC CFL CONDITION

Here, we derive a new CFL condition by finding a frequency associated with the nonlinear Lorentz force. This is done by finding the dispersion relation for the linearized momentum equation, temperature equation, and the magnetic induction equation (in its original form). We begin with the linearized momentum, temperature, and induction equation in the freefall nondimensionalisation,

$$\frac{\partial \mathbf{u}}{\partial t} + \nabla \mathbf{P} - T_1 \hat{\mathbf{z}} - \frac{1}{M_A^2} \mathbf{J} \times B_0 \hat{\mathbf{z}} = 0, \quad (\text{B1})$$

$$\frac{\partial \mathbf{B}}{\partial t} - \nabla \times (\mathbf{u} \times \mathbf{B}) = 0, \quad (\text{B2})$$

$$\frac{\partial \mathbf{T}}{\partial t} - (\mathbf{u} \cdot \nabla) T_0 = 0, \quad (\text{B3})$$

$$\nabla \cdot \mathbf{u} = 0, \quad (\text{B4})$$

$$\mathbf{J} - \nabla \times \mathbf{B} = 0, \quad (\text{B5})$$

where $\mathbf{u} = (u, v, w)$, M_A is the freefall Alfvénic Mach number, T_0 is the background temperature field, and T_1 is the perturbations about the background.

Substituting $\partial_t = i\omega$ and $\nabla = i(k_x\hat{\mathbf{x}} + k_y\hat{\mathbf{y}} + k_z\hat{\mathbf{z}})$ gives

$$i\omega u + ik_x P - \frac{1}{M_A^2} J_y B_0 = 0, \quad (\text{B6})$$

$$i\omega v + ik_y P + \frac{1}{M_A^2} J_x B_0 = 0, \quad (\text{B7})$$

$$i\omega w + ik_z P - T = 0, \quad (\text{B8})$$

$$i\omega Bx - ik_z B_0 u = 0, \quad (\text{B9})$$

$$i\omega By - ik_z B_0 v = 0, \quad (\text{B10})$$

$$i\omega Bz + ik_x B_0 u + ik_y B_0 v = 0, \quad (\text{B11})$$

$$i\omega T - w T_{0z} = 0, \quad (\text{B12})$$

$$ik_x u + ik_y v + ik_z w = 0, \quad (\text{B13})$$

$$J_x + ik_z B_y - ik_y B_z = 0, \quad (\text{B14})$$

$$J_y + ik_x B_z - ik_z B_x = 0, \quad (\text{B15})$$

$$J_z + ik_y B_x - ik_x B_y = 0, \quad (\text{B16})$$

where Eqs. (B6)–(B16) have been split into each directional component.

The dispersion relation is obtained by constructing a matrix system $\tilde{\mathbf{A}}\mathbf{x} = 0$, where \mathbf{x} is the vector of state variables, taking Eqs. (B6)–(B16) and setting the determinant equal to zero, $\text{Det}(\tilde{\mathbf{A}}) = 0$. This gives

$$\omega^4 + \omega^2(2f_A^2 - \xi N^2) - f_A^2 \xi N^2 + f_A^4 = 0, \quad (\text{B17})$$

where the Brunt-Vaisala frequency is $N^2 = T_{0z}$, and $\xi = k_\perp/k^2$, and the Alfvénic frequency $f_A = B_0 k_z / M_A$. This is the frequency associated with waves propagating along the background magnetic field; our timesteps are constrained by waves propagating along the instantaneous *fluctuations around the background* magnetic field. We estimate the frequency of these waves by replacing B_0 with the magnitude of these perturbations $|\mathbf{B}|$. So the characteristic frequency for the magnetic field fluctuations is

$$f_A = \frac{|\mathbf{B}|k_z}{M_A} = |\mathbf{B}|k_z \sqrt{\frac{Q\text{Pr}}{\text{Ra Pm}}}. \quad (\text{B18})$$

To implement this in Dedalus, a timestep was calculated for both the magnetic CFL and traditional advective CFL and the smallest of the two was used.

APPENDIX C: TABLES OF RUNS

Tables II–IX give details of the simulation suite, each table is at a fixed Q and Γ . As Q and Ra get larger, the simulations become more difficult, so we use a method called bootstrapping. We take the steady state of a lower Ra as initial conditions and increase the Ra . This skips the onset of convection, which is often the most difficult part of the simulation to resolve.

TABLE II. Run information for all runs at $Q = 10^4$, $\Gamma = 3.63$.

Ra	$N_x \times N_z$	Bootstrapped	s_{ml}	s_{mn}	s_i	s_b	s_v	Nu	Re	B_{rms}
2.4×10^5	128×256	—	0.06	0.033	0.0034	0.075	0.019	2.46	64.1	0.67
3×10^5	128×256	—	0.064	0.047	0.0089	0.079	0.021	3.13	89.0	0.84
3.55×10^5	128×256	—	0.068	0.054	0.0277	0.07	0.023	3.35	114.7	0.89
5×10^5	128×256	—	0.078	0.067	0.0393	0.071	0.022	3.82	144.5	1.28
7×10^5	128×256	—	0.077	0.073	0.0509	0.067	0.021	4.25	185.1	1.6
5×10^6	128×256	—	0.045	0.082	0.0978	0.045	0.016	6.68	689.8	4.55
7×10^6	128×256	—	0.04	0.092	0.1168	0.043	0.017	7.9	851.0	4.98
1×10^7	128×256	—	0.037	0.069	0.1139	0.044	0.016	8.8	917.2	5.92

 TABLE III. Run information for all runs at $Q = 10^5$, $\Gamma = 2.44$.

Ra	$N_x \times N_z$	Bootstrapped	s_{ml}	s_{mn}	s_i	s_b	s_v	Nu	Re	B_{rms}
2.4×10^6	128×256	—	0.085	0.057	0.0195	0.068	0.011	3.32	177.0	0.76
3×10^6	128×256	—	0.091	0.072	0.0306	0.065	0.013	4.21	241.0	0.87
3.55×10^6	128×256	—	0.089	0.074	0.0329	0.062	0.014	4.68	262.6	0.94
5×10^6	128×256	—	0.093	0.085	0.0442	0.061	0.015	5.9	345.6	1.18
7×10^6	128×256	—	0.094	0.092	0.0551	0.058	0.015	6.8	447.2	1.46
1×10^7	128×256	—	0.092	0.092	0.0647	0.054	0.015	7.62	576.9	1.78
3.55×10^7	256×512	—	0.065	0.086	0.0887	0.044	0.014	11.42	1116.4	3.46
5×10^7	256×512	—	0.059	0.085	0.0992	0.042	0.014	12.97	1395.6	3.93
7×10^7	256×512	—	0.052	0.082	0.1033	0.04	0.013	14.04	1647.2	4.56

 TABLE IV. Run information for all runs at $Q = 10^6$, $\Gamma = 1.64$.

Ra	$N_x \times N_z$	Bootstrapped	s_{ml}	s_{mn}	s_i	s_b	s_v	Nu	Re	B_{rms}
1.67×10^7	128×256	—	0.048	0.023	0.0013	0.047	0.004	2.98	226.5	0.42
2.36×10^7	128×256	—	0.046	0.027	0.0025	0.045	0.005	4.09	302.9	0.5
3.55×10^7	128×256	—	0.087	0.072	0.0277	0.053	0.008	6.9	674.1	0.85
5×10^7	128×256	3.55×10^7	0.098	0.089	0.0445	0.05	0.01	9.3	930.5	1.04
7×10^7	128×256	3.55×10^7	0.102	0.096	0.0542	0.048	0.011	11.58	1150.3	1.23
1×10^8	256×512	3.55×10^7	0.101	0.099	0.0673	0.043	0.011	12.68	1430.7	1.49
1.2×10^8	256×512	3.55×10^7	0.101	0.104	0.0696	0.043	0.011	13.66	1576.9	1.68
2×10^8	256×512	1×10^8	0.094	0.103	0.0821	0.04	0.01	15.9	2083.4	2.25
3.55×10^8	256×512	1×10^8	0.086	0.103	0.0994	0.038	0.01	20.21	2811.2	2.93
1.2×10^9	512×512	3.55×10^7	0.055	0.085	0.1023	0.029	0.009	27.25	4734.1	4.96
3.55×10^9	512×512	1.2×10^8	0.039	0.113	0.1413	0.026	0.009	49.38	8574.9	8.45

TABLE V. Run information for all runs at $Q = 10^7$, $\Gamma = 1.1$.

Ra	$N_x \times N_z$	Bootstrapped	s_{ml}	s_{mn}	s_i	s_b	s_v	Nu	Re	B_{rms}
1.67×10^8	128×256	1×10^7 ($Q = 10^6$)	0.04	0.018	0.0025	0.035	0.002	4.21	631.8	0.34
2.36×10^8	128×256	1.67×10^8	0.042	0.025	0.003	0.036	0.002	5.75	787.9	0.43
3×10^8	256×512	1.67×10^8	0.061	0.047	0.0128	0.039	0.004	8.4	1239.5	0.58
3.55×10^8	256×512	1.67×10^8	0.079	0.065	0.0235	0.043	0.005	9.94	1705.1	0.72
5×10^8	256×512	3.55×10^8	0.087	0.075	0.0343	0.04	0.005	12.55	2280.2	0.88
7×10^8	256×512	3.55×10^8	0.098	0.091	0.0508	0.037	0.007	17.4	3006.2	1.04
1×10^9	512×512	3.55×10^8	0.103	0.1	0.0592	0.034	0.007	18.64	3593.3	1.25
1.2×10^9	512×512	1×10^9	0.104	0.103	0.0653	0.033	0.007	20.72	4045.4	1.35
2×10^9	512×512	1×10^9	0.101	0.111	0.08	0.031	0.007	24.5	4909.2	1.78
3×10^9	512×512	1×10^9	0.097	0.123	0.0914	0.029	0.007	29.28	6127.5	2.17
3.55×10^9	512×512	1×10^9	0.095	0.147	0.0986	0.027	0.007	31.49	6854.4	2.33
5×10^9	512×512	1×10^9	0.08	0.117	0.0966	0.024	0.007	33.35	7814.5	2.43
7×10^9	512×512	1×10^9	0.076	0.149	0.1194	0.026	0.007	44.69	9656.8	3.35
1×10^{10}	1024×1024	1.2×10^9	0.064	0.147	0.1125	0.022	0.006	37.98	10413.7	4.01
1.2×10^{10}	1024×1024	1.2×10^9	0.061	0.187	0.1368	0.021	0.006	38.37	11309.0	3.82

 TABLE VI. Run information for all runs at $Q = 10^8$, $\Gamma = 0.74$.

Ra	$N_x \times N_z$	Bootstrapped	s_{ml}	s_{mn}	s_i	s_b	s_v	Nu	Re	B_{rms}
1.67×10^9	256×512	3.55×10^8 ($Q = 10^7$)	0.035	0.016	0.0035	0.025	0.001	5.75	1780.8	0.29
2.36×10^9	256×512	1.67×10^9	0.04	0.025	0.0048	0.027	0.002	8.37	2428.0	0.38
3×10^9	256×512	1.67×10^9	0.046	0.034	0.0058	0.03	0.002	10.66	3076.3	0.48
3.55×10^9	256×512	1.67×10^9	0.053	0.042	0.0112	0.028	0.002	13.7	3583.1	0.52
5×10^9	256×512	3.55×10^9	0.074	0.064	0.0245	0.028	0.004	21.13	5823.9	0.71
7×10^9	256×512	3.55×10^9	0.083	0.076	0.0345	0.027	0.004	26.31	7208.2	0.82
1×10^{10}	512×512	7×10^9	0.097	0.093	0.053	0.026	0.005	32.46	9057.4	1.0
1.2×10^{10}	512×512	1×10^{10}	0.098	0.102	0.0559	0.025	0.005	33.69	9632.2	1.06
2×10^{10}	512×512	1×10^{10}	0.104	0.148	0.0773	0.023	0.006	43.96	12455.4	1.34
3×10^{10}	512×512	2×10^{10}	0.104	0.209	0.1067	0.021	0.006	46.95	16509.9	1.73
3.55×10^{10}	512×512	2×10^{10}	0.101	0.244	0.1124	0.021	0.006	51.7	16211.1	1.75
1×10^{11}	512×512	3.55×10^{10}	0.087	0.279	0.1408	0.019	0.006	97.73	25587.8	2.69

 TABLE VII. Run information for all runs at $Q = 10^9$, $\Gamma = 0.5$.

Ra	$N_x \times N_z$	Bootstrapped	s_{ml}	s_{mn}	s_i	s_b	s_v	Nu	Re	B_{rms}
1.67×10^{10}	256×512	3.55×10^9 ($Q = 10^8$)	0.029	0.013	0.0038	0.018	0.001	7.79	4667.9	0.23
2.36×10^{10}	256×512	1.67×10^{10}	0.033	0.02	0.0045	0.02	0.001	11.4	6260.2	0.31
3×10^{10}	256×512	1.67×10^{10}	0.037	0.025	0.0054	0.021	0.001	14.66	7460.9	0.37
3.55×10^{10}	256×512	1.67×10^{10}	0.04	0.031	0.008	0.021	0.001	17.29	8632.3	0.42
5×10^{10}	512×512	3.55×10^{10}	0.055	0.048	0.0169	0.021	0.002	27.93	12719.9	0.55
1×10^{11}	512×512	5×10^{10}	0.086	0.106	0.0442	0.019	0.003	50.53	22861.0	0.81
1.5×10^{11}	512×1024	1×10^{11}	0.098	0.107	0.0577	0.017	0.004	61.34	28750.0	0.95
2×10^{11}	1024×1024	1.5×10^{11}	0.103	0.191	0.074	0.017	0.004	69.11	31694.4	1.09
2.5×10^{11}	1024×1024	2×10^{11}	0.111	0.2	0.0892	0.017	0.004	91.3	37940.6	1.26
3×10^{11}	1024×1024	2.5×10^{11}	0.112	0.225	0.0885	0.016	0.004	94.07	41269.6	1.3
3.55×10^{11}	1024×1024	3×10^{11}	0.117	0.225	0.1158	0.015	0.004	83.51	42131.1	1.42

TABLE VIII. Run information for all runs at $Q = 10^{10}$, $\Gamma = 0.33$.

Ra	$N_x \times N_z$	Bootstrapped	s_{ml}	s_{mn}	s_i	s_b	s_v	Nu	Re	B_{rms}
1.67×10^{11}	256×512	3.55×10^{10} ($Q = 10^9$)	0.024	0.014	0.0044	0.012	0.0	10.21	9716.4	0.16
2.36×10^{11}	256×512	1.67×10^{11}	0.024	0.015	0.0038	0.012	0.0	11.47	10229.1	0.18
3×10^{11}	256×512	1.67×10^{11}	0.034	0.026	0.0055	0.014	0.001	21.68	15087.2	0.29
3.55×10^{11}	512×512	1.67×10^{11}	0.036	0.029	0.0064	0.014	0.001	27.43	17114.3	0.33
5×10^{11}	512×1024	3.55×10^{11}	0.048	0.043	0.017	0.014	0.001	39.27	26520.8	0.41
7×10^{11}	512×1024	5×10^{11}	0.06	0.064	0.0214	0.015	0.001	60.44	33605.0	0.55
1×10^{12}	1024×2048	7×10^{11}	0.076	0.074	0.0274	0.015	0.002	54.08	45429.6	0.69

 TABLE IX. Run information for all 3D runs at $Q = 10^6$, $\Gamma = 1.64$.

Ra	$N_x \times N_y \times N_z$	Bootstrapped	s_{ml}	s_{mn}	s_i	s_b	s_v	Nu	Re	B_{rms}
1.67×10^7	$64 \times 64 \times 128$	—	0.056	0.031	0.0086	0.045	0.005	3.38	263.3	0.43
3.55×10^7	$64 \times 64 \times 128$	1.67×10^7	0.063	0.083	0.0461	0.04	0.012	7.95	527.2	0.59
7×10^7	$64 \times 64 \times 128$	3.55×10^7	0.092	0.172	0.1267	0.044	0.021	16.14	1281.3	1.04
1×10^9	$512 \times 512 \times 512$	7×10^7	0.088	0.242	0.3096	0.022	0.027	13.72	5283.2	3.47

- [1] J. MacDonald and D. J. Mullan, Magnetic modeling of inflated low-mass stars using interior fields no larger than ~ 10 kG, *Astrophys. J.* **850**, 58 (2017).
- [2] M. Cantiello and J. Braithwaite, Magnetic spots on hot massive stars, *Astron. Astrophys.* **534**, A140 (2011).
- [3] R. Raynaud, P. Cerdá-Durán, and J. Guilet, Gravitational wave signature of proto-neutron star convection: I. MHD numerical simulations, *Mon. Not. R. Astron. Soc.* **509**, 3410 (2021).
- [4] L. E. Held and H. N. Latter, Magnetohydrodynamic convection in accretion discs, *Mon. Not. R. Astron. Soc.* **504**, 2940 (2021).
- [5] S. V. Starchenko, Supercritical magnetoconvection in rapidly rotating planetary cores, *Phys. Earth Planet. Inter.* **117**, 225 (2000).
- [6] B. P. Brown, M. S. Miesch, M. K. Browning, A. S. Brun, and J. Toomre, Magnetic cycles in a convective dynamo simulation of a young solar-type star, *Astrophys. J.* **731**, 69 (2011).
- [7] N. O. Weiss, D. P. Brownjohn, P. C. Matthews, and M. R. E. Proctor, Photospheric convection in strong magnetic fields, *Mon. Not. R. Astron. Soc.* **283**, 1153 (1996).
- [8] J. H. Thomas and N. O. Weiss, Fine structure in sunspots, *Annu. Rev. Astron. Astrophys.* **42**, 517 (2004).
- [9] D. Orozco Suárez, L. R. Bellot Rubio, J. C. del Toro Iniesta, and S. Tsuneta, Magnetic field emergence in quiet sun granules, *Astron. Astrophys.* **481**, L33 (2008).
- [10] R. Schlichenmaier, O. von der Lühse, S. Hoch, D. Soltau, T. Berkefeld, D. Schmidt, W. Schmidt, C. Denker, H. Balthasar, A. Hofmann *et al.*, Active region fine structure observed at 0.08 arcsec resolution, *Astron. Astrophys.* **596**, A7 (2016).
- [11] M. R. E. Proctor and N. O. Weiss, Magnetoconvection, *Rep. Prog. Phys.* **45**, 1317 (1982).
- [12] M. Schüssler, S. Shelyag, S. Berdyugina, A. Vögler, and S. K. Solanki, Why solar magnetic flux concentrations are bright in molecular bands, *Astrophys. J.* **597**, L173 (2003).
- [13] M. Carlsson, R. F. Stein, Å. Nordlund, and G. B. Scharmer, Observational manifestations of solar magnetoconvection: Center-to-limb variation, *Astrophys. J.* **610**, L137 (2004).

- [14] J. H. Thomas and N. O. Weiss, *Sunspots: Theory and Observation* (Kluwer Academic Publishing, Dordrecht, 1992).
- [15] T. G. Cowling, *The Sun, the Solar System*, Vol. 1, edited by Gerard P. Kuiper (University of Chicago Press, Chicago, IL, 1953), pp. xix, 745, [Quart. J. Roy. Meteorol. Soc. **83**, 137 \(1953\)](#).
- [16] W. Deinzer, On the magneto-hydrostatic theory of sunspots, [Astrophys. J. **141**, 548 \(1965\)](#).
- [17] M. Schüssler and A. Vogler, Magneto-convection in a sunspot umbra, [Astrophys. J. **641**, L73 \(2006\)](#).
- [18] L. Bharti, R. Jain, and S. Jaaffrey, Evidence for magnetoconvection in sunspot umbral dots, [Astrophysical J. **665**, L79 \(2007\)](#).
- [19] M. Schüssler (Ed.), Numerical simulation of solar magneto-convection in *Advanced Solar Polarimetry – Theory, Observation, and Instrumentation – 20TH NSO/Sac Summer Workshop*, ASP Conference Proceedings Vol. 236 (Astronomical Society of the Pacific, 2001), p. 343.
- [20] N. O. Weiss, Modelling stellar magnetoconvection, [Sympos. Int. Astron. Union **210**, 127 \(2003\)](#).
- [21] P. J. Bushby and S. M. Houghton, Spatially intermittent fields in photospheric magnetoconvection, [Mon. Not. R. Astron. Soc. **362**, 313 \(2005\)](#).
- [22] M. Schmassmann, M. Rempel, N. Bello González, R. Schlichenmaier, and J. Jurčák, Characterization of magneto-convection in sunspots: The Gough-Tayler stability criterion in MURaM sunspot simulations, [Astron. Astrophys. **656**, A92 \(2021\)](#).
- [23] F. Cattaneo, T. Emonet, and N. Weiss, On the interaction between convection and magnetic fields, [Astrophys. J. **588**, 1183 \(2003\)](#).
- [24] N. Weiss, M. Proctor, and D. Brownjohn, Magnetic flux separation in photospheric convection, [Mon. Not. R. Astron. Soc. **337**, 293 \(2002\)](#).
- [25] L. Tao, M. R. E. Proctor, and N. O. Weiss, Flux expulsion by inhomogeneous turbulence, [Mon. Not. R. Astron. Soc. **300**, 907 \(1998\)](#).
- [26] J. M. Aurnou, S. Horn, and K. Julien, Connections between nonrotating, slowly rotating, and rapidly rotating turbulent convection transport scalings, [Phys. Rev. Res. **2**, 043115 \(2020\)](#).
- [27] S. Stellmach, M. Lischper, K. Julien, G. Vasil, J. S. Cheng, A. Ribeiro, E. M. King, and J. M. Aurnou, Approaching the Asymptotic Regime of Rapidly Rotating Convection: Boundary Layers Versus Interior Dynamics, [Phys. Rev. Lett. **113**, 254501 \(2014\)](#).
- [28] K. Julien, A. M. Rubio, I. Grooms, and E. Knobloch, Statistical and physical balances in low Rossby number Rayleigh-Bénard convection, [Geophys. Astrophys. Fluid Dyn. **106**, 392 \(2012\)](#).
- [29] M. Plumley and K. Julien, Scaling laws in Rayleigh-Bénard convection, [Earth Space Sci. **6**, 1580 \(2019\)](#).
- [30] E. H. Anders, C. M. Manduca, B. P. Brown, J. S. Oishi, and G. M. Vasil, Predicting the Rossby number in convective experiments, [Astrophys. J. **872**, 138 \(2019\)](#).
- [31] J. M. Aurnou and P. L. Olson, Experiments on Rayleigh-Bénard convection, magnetoconvection and rotating magnetoconvection in liquid gallium, [J. Fluid Mech. **430**, 283 \(2001\)](#).
- [32] U. Burr and U. Müller, Rayleigh-Bénard convection in liquid metal layers under the influence of a vertical magnetic field, [Phys. Fluids **13**, 3247 \(2001\)](#).
- [33] T. Zürner, F. Schindler, T. Vogt, S. Eckert, and J. Schumacher, Flow regimes of Rayleigh-Bénard convection in a vertical magnetic field, [J. Fluid Mech. **894**, A21 \(2020\)](#).
- [34] A. M. Grannan, J. S. Cheng, A. Aggarwal, E. K. Hawkins, Y. Xu, S. Horn, J. Sánchez-Álvarez, and J. M. Aurnou, Experimental pub crawl from Rayleigh-Bénard to magnetostrophic convection, [J. Fluid Mech. **939**, R1 \(2022\)](#).
- [35] X. Yu, J. Zhang, and M.-J. Ni, Numerical simulation of the Rayleigh-Benard convection under the influence of magnetic fields, [Int. J. Heat Mass Transf. **120**, 1118 \(2018\)](#).
- [36] S. Cioni, S. Chaumat, and J. Sommeria, Effect of a vertical magnetic field on turbulent Rayleigh-Bénard convection, [Phys. Rev. E **62**, R4520\(R\) \(2000\)](#).
- [37] M. Yan, M. Calkins, S. Maffei, K. Julien, S. Tobias, and P. Marti, Heat transfer and flow regimes in quasi-static magnetoconvection with a vertical magnetic field, [J. Fluid Mech. **877**, 1186 \(2019\)](#).
- [38] R. Akhmedageev, O. Zikanov, D. Krasnov, and J. Schumacher, Rayleigh-Bénard convection in strong vertical magnetic field: Flow structure and verification of numerical method, [Magnetohydrodynamics **56**, 157 \(2020\)](#).

- [39] B. Knaepen and R. Moreau, Magnetohydrodynamic turbulence at low magnetic Reynolds number, *Annu. Rev. Fluid Mech.* **40**, 25 (2008).
- [40] A. S. Jermyn, E. H. Anders, D. Lecoanet, and M. Cantiello, An atlas of convection in main-sequence stars, *ApJS* **262**, 19 (2022).
- [41] P. Charbonneau, Dynamo models of the solar cycle, *Liv. Rev. Solar Phys.* **7**, 3 (2010).
- [42] R. J. Teed and E. Dormy, Solenoidal force balances in numerical dynamos, *J. Fluid Mechanics*, **964** (2023).
- [43] D. W. Hughes and F. Cattaneo, Force balance in convectively driven dynamos with no inertia, *J. Fluid Mech.* **879**, 793 (2019).
- [44] N. Hurlburt and A. Rucklidge, Development of structure in pores and sunspots: Flows around axisymmetric magnetic flux tubes, *Mon. Not. R. Astron. Soc.* **314**, 793 (2000).
- [45] B. Brown, Dynamos in stellar convection zones: Of wreaths and cycles, *J. Phys.: Conf. Ser.* **271**, 012064 (2011).
- [46] E. H. Anders, D. Lecoanet, and B. P. Brown, Entropy rain: Dilution and compression of thermals in stratified domains, *Astrophys. J.* **884**, 65 (2019).
- [47] S. Chandrasekhar, *Hydrodynamic and Hydromagnetic Stability* (Clarendon Press, Oxford, UK, 1961).
- [48] N. Tarshish, N. Jeevanjee, and D. Lecoanet, Buoyant motion of a turbulent thermal, *J. Atmos. Sci.* **75**, 3233 (2018).
- [49] K. J. Burns, G. M. Vasil, J. S. Oishi, D. Lecoanet, and B. P. Brown, Dedalus: A flexible framework for numerical simulations with spectral methods, *Phys. Rev. Res.* **2**, 023068 (2020).
- [50] U. M. Ascher, S. J. Ruuth, and R. J. Spiteri, Implicit-explicit Runge-Kutta methods for time-dependent partial differential equations, *Appl. Numer. Math.* **25**, 151 (1997), special Issue on Time Integration.
- [51] J. S. Oishi, K. J. Burns, S. E. Clark, E. H. Anders, B. P. Brown, G. M. Vasil, and D. Lecoanet, eigentools: A python package for studying differential eigenvalue problems with an emphasis on robustness, *J. Open Source Softw.* **6**, 3079 (2021).
- [52] P. C. Matthews, Asymptotic solutions for nonlinear magnetoconvection, *J. Fluid Mech.* **387**, 397 (1999).
- [53] T. Vogt, S. Horn, and J. M. Aurnou, Oscillatory thermal-inertial flows in liquid metal rotating convection, *J. Fluid Mech.* **911**, A5 (2021).
- [54] See Supplemental Material at <http://link.aps.org/supplemental/10.1103/PhysRevFluids.8.093503> for all simulation data, including solenoidal force values, Nusselt number, Reynolds number, and average magnetic field.
- [55] https://github.com/imogencresswell/boussinesq_convection.git.
- [56] X. Zhu, V. Mathai, R. J. A. M. Stevens, R. Verzicco, and D. Lohse, Transition to the ultimate regime in two-dimensional Rayleigh-Bénard convection, *Phys. Rev. Lett.* **120**, 144502 (2018).
- [57] G. Ahlers, S. Grossmann, and D. Lohse, Heat transfer and large scale dynamics in turbulent Rayleigh-Bénard convection, *Rev. Mod. Phys.* **81**, 503 (2009).
- [58] C. Guervilly, P. Cardin, and N. Schaeffer, Turbulent convective length scale in planetary cores, *Nature (London)* **570**, 368 (2019).
- [59] K. Julien, S. Legg, J. McWilliams, and J. Werne, Rapidly rotating turbulent Rayleigh-Bénard convection, *J. Fluid Mech.* **322**, 243 (1996).
- [60] K. Julien, S. Legg, J. McWilliams, and J. Werne, Hard turbulence in rotating Rayleigh-Bénard convection, *Phys. Rev. E* **53**, R5557(R) (1996).
- [61] J. Werne, Structure of hard-turbulent convection in two dimensions: Numerical evidence, *Phys. Rev. E* **48**, 1020 (1993).